ScienceAdvances AAAS

Manuscript Template

FRONT MATTER

Title

Long title

Innovative qPCR using interfacial effects to enable low threshold cycle detection and inhibition relief

Short title

Innovative qPCR using interfacial effects

Authors

Dustin K. Harshman,[1] Brianna M. Rao,[2] Jean E. McLain,[3] George S. Watts,[4] Jeong-Yeol Yoon[1,2,5]*

Affiliations

[1]Biomedical Engineering Graduate Interdisciplinary Program, The University of Arizona, Tucson, USA.
[2]Department of Biomedical Engineering, The University of Arizona, Tucson, USA.
[3]Water Resources Research Center and Department of Soil, Water and Environmental Science, The University of Arizona, Tucson, USA.
[4]Arizona Cancer Center and Department of Pharmacology, The University of Arizona, Tucson, USA.
[5]Department of Agricultural and Biosystems Engineering, The University of Arizona, Tucson, USA.
*Correspondence should be addressed to J.Y.Y. (jyyoon@email.arizona.edu).

Abstract

Molecular diagnostics offer quick access to information but fail to operate at speeds required for clinical decision-making. Our novel methodology, *droplet-on-thermocouple silhouette real-time polymerase chain reaction* (DOTS qPCR), uses interfacial effects for droplet actuation, inhibition relief, and amplification sensing. DOTS qPCR has sample-to-answer times as short as 3 min 30 s. Towards diagnosing infective endocarditis, we demonstrate the following: reproducibility, differentiation of antibiotic susceptibility, sub-picogram limit of detection, and thermocycling speeds of up to 28 s/cycle in the presence of tissue contaminants. Langmuir and Gibbs adsorption isotherms are used to describe the decreasing interfacial tension upon amplification. Moreover, a log-linear relationship with low threshold cycles is presented for real-time quantification by imaging the droplet-on-thermocouple silhouette with a smartphone. DOTS qPCR resolves several limitations of commercially available real-time PCR systems, which rely on fluorescence detection, have substantially higher threshold cycles, and require expensive optical components and extensive sample preparation. Because of the advantages of low threshold cycle detection, we anticipate extending this technology to biological research applications such as single cell, single nucleus, and single DNA molecule analyses. Our work is the first demonstrated use of interfacial effects for sensing reaction progress, and it will enable point-of-care molecular diagnosis of infections.

Keywords: antibiotic resistance, infective endocarditis, real-time PCR, interfacial tension, inhibition relief, emulsification, rapid molecular diagnostics, point-of-care, sample-to-answer

MAIN TEXT

Introduction

Two years after the U.S. Food and Drug Administration (FDA) approved methicillin, methicillin-resistant *Staphylococcus aureus* (MRSA) emerged (*1*). This rapid emergence demonstrates the speed of bacterial evolution in response to selective pressures. Vancomycin is the standard of care and last resort for treating MRSA (*2–4*), but vancomycin-resistant enterococci (VRE) have also appeared in the clinic (*5*). VRE contain a 10.8-kb transposon, Tn*1546* (*2, 6*), which carries the ligase-encoding gene *vanA* (*7*). Tn*1546* has transconjugated from enterococci to MRSA on at least 12 independent clinical occasions (*3, 8–10*), resulting in vancomycin-resistant *Staphylococcus aureus* (VRSA) (*11)*. Due to its low incidence, VRSA is currently designated as a "concerning threat" by the U.S. Centers for Disease Control and Prevention (CDC) *(12*). Currently, streptococci, enterococci, and *Staphylococcus aureus* are the three most common causative agents of infective endocarditis (IE) (*13*). VRE and MRSA co-exist in clinics (*14*), especially in severe IE cases (*15*), and more than one-fourth of MRSA isolates from IE cases show tolerance to vancomycin (*16*). Despite medical advancements, this microbial ecology impedes disease management and results in increased levels of morbidity and mortality (*17*). The rapid emergence of vancomycin-resistant bacteria undermines our ability to treat serious infections and highlights the urgent need for technological innovation to allow widespread surveillance of antibiotic resistance dissemination.

Traditional methods of IE diagnosis include transesophogeal echocardiography and culture of blood heart valve tissues (*17*). Rapid diagnosis of IE followed by immediate and directed therapy represents the best standard of clinical care (*18*). Therefore, there has been great interest in molecular diagnostics, including gene-specific polymerase chain reaction (PCR) and 16S rRNA hypervariable region PCR (*19*). Although these approaches have been shown to substantially improve diagnostic outcomes (*15, 20–23*), empiric antibiotic therapy has to be initiated while the test results are awaited (*24*). Empiric therapy is guided by practical experience and is administered before a definitive diagnosis has been made. However, empiric therapy can complicate disease management by diminishing the protective flora and selecting for resistance (*25*). To alleviate the need for empiric therapy, new technologies are being developed to decrease the time required for diagnosis. For example, the Roche LightCycler can detect 25 clinically important pathogens from whole blood within 6 h (*26*), the Cepheid GeneXpert can quickly detect *S. aureus* genomic DNA from whole blood (*27*), and the Accelerate ID/AST system can identify causative pathogens and determine susceptibility phenotypes within 4 h (*28*). IE presents a unique opportunity for the implementation of rapid molecular diagnostics because the vegetations have highly concentrated, slow-growing bacterial populations compared with bacteremia (*17*). However, the presence of PCR inhibitors in biopsy samples, obtained through valve excision or by endoscopic bioptome, presents challenges to PCR-based tests.

Within the clinical setting, a physician's decision-making window is generally less than 10 min, which often leads to empiric rather than targeted therapy. Therefore, a specific challenge within this context is matching the sample-to-answer time with the decision-making time. As participants in this race against bacterial evolution, we have developed a droplet-based real-time PCR device. Our novel method relies on interfacial effects for droplet actuation, PCR inhibitor compartmentalization, and amplification sensing. Droplet actuation for conducting PCR has been previously achieved by employing electrowetting-on-dielectric (EWOD) principles (*29*) and by

using lab-on-a-chip platforms with droplets flowing in microchannels (*30*). Another similar technique has used a nanostructured surface to minimize surface fouling and enable repeated droplet manipulations (*31*). Although the fluid dynamics required for droplet actuation in automated rapid assays have been studied extensively, sensing modalities have been limited to fluorescence, colorimetry, surface plasmon resonance, and electrochemistry. In our approach, repeated droplet manipulations are achieved without surface fouling, and sensitive detection at early PCR thermal cycles is made possible by an novel sensing modality based on interfacial effects.

In this study, we demonstrate the ability of our methodology, *droplet-on-thermocouple silhouette real-time PCR* (DOTS qPCR), to provide the following important features: 1) thermocycling times that are as fast as 28 s/cycle; 2) elimination of evaporation by silicone oil immersion of the reaction droplet; 3) stabilization of the droplet-on-thermocouple by interfacial tension; 4) compartmentalization of contaminating proteins at the oil–water interface, thereby relieving their inhibitory effects on PCR (inhibition relief); 5) sub-picogram limit of detection; and 6) detection of amplification in 3 min 30 s. In DOTS qPCR, amplification is detected by measuring the decrease in droplet volume caused by the changing interfacial composition. This innovative qPCR detection method enables detection as early as the fourth thermal cycle, which is unachievable by the measurement of fluorescence that qPCR has relied upon for decades. The performance of our method is demonstrated here using the 16S rRNA gene V3 hypervariable region and the *vanA* gene for amplification. Most importantly, DOTS qPCR has a sample-to-answer time within the physician's decision-making window, allowing for informed decision-making.

Results

The droplet-on-thermocouple silhouette real-time PCR (DOTS qPCR) device

We designed the DOTS qPCR device (Figs. 1A,B) to be readily deployed as a point-of-care diagnostic tool and to epitomize simplicity, small form factor, mobile integration, and disposability. The droplet-on-thermocouple (DOT) (Fig. 1C) is submerged in a heated oil environment and is positioned by a motor (Figs. 1D–F and Movies S1–S4). The oil is contained within a semicircular channel with two heaters, located at 0° and 180°, which maintain the two temperature extremes (45–50°C and 100–105°C). A heat gradient is established along the channel with temperatures between the two extremes being represented (Fig. 2A). From room temperature (25°C), the steady state of the heat gradient is established within 10 min of commencing temperature ramping using proportional-integral-derivative (PID) control of the heater power (Fig. 2B). At the midpoint of the channel, a viewing window allows macroscopic imaging of the droplet by a smartphone camera with an attached lens. The oil temperature at this window is 70°C. The internal temperature of the droplet is continuously monitored by a thermocouple, which is bent such that the thermocouple junction is positioned inside the droplet (Fig. 1C). The position of the droplet within the heat gradient is accurately controlled using real-time feedback of its internal temperature.

Non-specific amplification is avoided by dispensing the droplet onto the thermocouple loop at the 50°C region of the gradient. Rapid thermocycling is then conducted by continuously moving the droplet within the heated oil until the desired temperature is reached (Figs. 1D–F and Movies S3, S4). This continuous movement enhances the thermal transfer since it provides forced convection between the droplet and the oil (*32*). By this technique, droplet ramp rates up to

12°C/s and oil ramp rates up to 32°C/s are achieved (Fig. 2C). Thermal cycle times range from 28 to 48 s, depending on the desired mode of operation. The thermocycling temperature profiles indicate that reaction temperatures are consistently achieved in each cycle (Fig. 2C). The droplet temperatures at each phase are 90.4 ± 0.2°C for denaturation, 68.4 ± 0.2°C for extension, and 60.2 ± 0.2°C for annealing. The accuracy of the temperature control is ensured by real-time droplet temperature feedback.

In order to decrease thermal cycle times, increased offsets between the oil temperature and the desired droplet temperature ($T_{oil} - T_{droplet}$) are used to enhance convective heat transfer. Convective heat transfer is governed by the equation, $q = h(T_\infty - T_{object})$, where q is heat flux, h is the heat transfer coefficient, T_∞ is the temperature of the surrounding medium (the oil), and T_{object} is the temperature of the object being heated (the droplet). To achieve the temperature offsets, the droplet is positioned at oil temperatures higher than the desired droplet temperature during heating and at oil temperatures lower than the desired droplet temperature during cooling (Fig. 2C). Greater offsets yield a more rapid rate of heat transfer, and droplet temperature feedback is used to mitigate the risk of overshoot. Using this thermocycling strategy, we observed reproducible amplification of the hypervariable region V3 of the 16S rRNA gene from 7 pg purified *Klebsiella pneumoniae* genomic DNA (equivalent to 1.4×10^3 genomic copies) at thermocycling speeds of 48 s/cycle (Fig. 2D). The coefficient of variation of the three band intensities, representing three separate amplifications, is 4.0%, indicating a high degree of consistency between measurements. The absence of a band for the no template control (NTC) (Fig. 2D) indicates that the device is not susceptible to DNA contamination, which could lead to false positives.

Interfacial adsorption of contaminating tissue proteins

A porcine model for IE was developed (*33*) (Fig. 3F). Excised heart valve tissue punches (6 mm diameter sections) (Fig. 3G) were sterilized, inoculated with vancomycin-resistant *Enterococcus faecium* (VRE), and ground using a micro-mortar and -pestle. The liquid phase of the tissue after grinding had a protein concentration of 1.6 ± 0.1 mg/mL (Fig. 3A). The interfacial tensions (γ) of the PCR cocktail with the purified target and the PCR cocktail with the tissue-contaminated target were measured with a First Ten Ångstroms (FTÅ) 200 contact angle and interfacial tension analyzer, and the interfacial tensions were 25.55 mN/m and 27.60 mN/m, respectively (Fig. 3B). A free-body force diagram illustrates the direction of the forces acting on the droplet-on-thermocouple (Fig. 3C). Due to the interfacial tension force F_γ, a droplet of the PCR mixture can be suspended on the thermocouple loop. In fluorescence qPCR, tissue proteins inhibit amplification of the 16S rRNA gene V1–V2 hypervariable regions and the antibiotic resistance gene *vanA* from intact VRE. Therefore, the threshold cycles (C_t) are shifted upward by 1.6 cycles for the 16S rRNA V1–V2 reaction and by 5.4 cycles for the *vanA* reaction (Fig. 3D). In DOT thermocycling, these tissue proteins should be adsorbed at the oil–water interface, so that contaminating proteins are effectively eliminated from the PCR (interfacial compartmentalization). However, *Taq* polymerase should not be adsorbed at the oil–water interface. Therefore, the diffusion amounts of the relevant blood and tissue proteins (*34*) to the oil–water interface were calculated for comparison with the diffusion of *Taq* polymerase (Fig. 3E). The following proteins were included in the calculation, with the corresponding molecular weights and diffusivities: albumin (94 kDa, 6.1×10^{-7}), immunoglobulin-G (150 kDa, 4.0×10^{-7} cm^2/s), fibrinogen (340 kDa, 2.0×10^{-7} cm^2/s) (*35*), fibronectin (450 kDa, 0.9×10^{-7} cm^2/s) (*36*), collagen type I (282 kDa, 0.78×10^{-7} cm^2/s) (*37*), tropoelastin (65 kDa, 4.6×10^{-7} cm^2/s) (*38*), and *Taq* polymerase (94 kDa, 4.7×10^{-7} cm^2/s) (*39*). As shown in Figure 3G, the adsorbed

amounts of albumin and fibrinogen are several orders of magnitude greater than that of *Taq* polymerase.

Amplification performance of droplet-on-thermocouple (DOT) thermocycling

Vancomycin-resistant *Enterococcus faecium* (VRE) and vancomycin-sensitive *Enterococcus faecalis* (VSE) were successfully distinguished based on amplification of a 377 bp segment of the *vanA* gene directly from bacterial culture using DOT thermocycling (Fig. 4A). This band was absent for the no template control (NTC) sample. A sub-picogram limit of detection (LOD) was established for amplification of the 196 bp 16S rRNA V3 amplicon from 0.7 pg *K. pneumoniae* genomic DNA (equivalent to 1.4×10^2 genomic copies) at 48 s/cycle (Fig. 4B). Moreover, the plasmid-mediated antibiotic resistance gene *vanA* was amplified directly from the inoculated heart valve tissue (Fig. 4C lane 1). The inoculum contained 7×10^5 colony-forming units (CFU) of VRE, which is in the concentration range relevant to IE vegetations (*40*). The inoculated heart valve tissue was ground with micro-mortar and -pestle, and the liquid phase was pipetted directly into the PCR cocktail without further purification. Despite inhibitions observed on the fluorescence qPCR instrument, amplification in the presence of protein contamination was achieved, because of interfacial compartmentalization (leading to inhibition relief) (*41*). The 16S rRNA V3 region was successfully amplified from the inoculated heart valve tissue at thermocycling speeds of up to 28 s/cycle or 14 min/30 cycles (Fig. 4C lanes 2–4).

Real-time detection by analysis of droplet-on-thermocouple silhouette

We observed that PCR amplification in the presence of SYBR Green I (SG) by DOT thermocycling is accompanied by a change in droplet volume, which is measured as a change in droplet height from the initial value before thermocycling. The change in volume is observed through the viewing window at the 70°C region of the heat gradient. Images are captured by the smartphone camera every 5 cycles (Fig. 5B), and the droplet-on-thermocouple silhouette is used for droplet height measurements. During the early thermal cycles, the decrease in droplet volume is dependent on the initial DNA amount (N_0) of the reaction (Fig. 5A).

In Figure 5A, the percent decrease in droplet height is plotted against the cycle number (C_n) for N_0 values ranging from 1.5×10^2 to 1.5×10^5 genomic copies. The error bars of the droplet height measurements represent the overall device noise, which was determined by loading consecutive 7.5 µL droplets onto the thermocouple loop, positioning the droplet-on-thermocouple at the viewing window, imaging the droplet with the smartphone camera, and measuring the standard error of the droplet height measurement. The detection threshold (4.8% decrease in droplet height) is also plotted in the figure to illustrate how C_t can be calculated by linear interpolation between two measured values. The threshold value of 4.8% was chosen to optimize the R^2 value of the standard curve linear regression.

Decrease in interfacial tension during amplification in the presence of SYBR Green I

To compare the interfacial tension of PCR mixtures during amplification with the signals from gel electrophoresis and fluorescence qPCR, the following experiments were performed. First, a PCR with 1.5×10^4 genomic copies was conventionally thermocycled with SG in increments of 5 thermal cycles, and the amplification was analyzed by gel electrophoresis (Fig. S1A). Another PCR with the same N_0 (1.5×10^4 genomic copies) was similarly thermocycled but in the absence of SG (Fig. S1B). A third PCR lacking target DNA (NTC) was thermocycled with SG, and no

amplification was detectable by gel electrophoresis even after 30 thermal cycles (Fig. S1C). The band intensities on the gel electropherograms were quantified at the expected product length (196 bp), normalized to the band intensity at C_0, and plotted against C_n (Fig. 6A). DNA amplification was detected after 20 thermal cycles by gel electrophoresis and after 21.11 ± 0.06 thermal cycles by fluorescence (Fig. 6B) for the reactions with N_0 of 1.5×10^4 genomic copies. No amplification was detected for the NTC reaction with SG by gel electrophoresis or by fluorescence.

The interfacial tension γ during the three different reactions was measured every 5 thermal cycles with a First Ten Ångstroms (FTÅ) 200 contact angle and interfacial tension analyzer. The change in interfacial tension with respect to the interfacial tension at C_0 ($d\gamma/\gamma_0$) was plotted against C_n (Fig. 6C). The interfacial tension of the SG reaction with amplification decreased by 21% by C_{10}, after which it remained nearly constant. On the other hand, the interfacial tension of the SG NTC reaction increased by 6% at C_5 and thereafter subsequently fluctuated within 4% of no change. The interfacial tension of the reaction with amplification but without SG increased by 11% at C_5 and then increased to 19% by C_{30}. The only reaction condition that resulted in an appreciable decrease in the interfacial tension as a function of C_n was the combination of SG and an increasing DNA concentration (Fig. 6C). Interestingly, after DNA amplification by PCR in the presence of SG, colloidal suspensions within the oil phase were observed by light microscopy (Fig. 7A). These water-in-oil droplets have a volume of 0.5–4.2 fL and a corresponding diameter of 1–2 μm.

Low threshold cycle detection by DOTS qPCR

In order to establish a standard curve, the logarithm of the initial DNA amount [$\log(N_0)$] is plotted against the threshold cycle C_t in Figure 8. The threshold cycle is defined as the theoretical fractional thermal cycle at which the detection threshold is reached. The detection threshold for DOTS qPCR (Fig. 8A) was set at a 4.8% decrease in droplet height, and the C_t values were calculated by linear interpolation between two measured values. For fluorescence qPCR (Fig. 8B), the detection threshold was set at 1.0, and the C_t values were calculated using the StepOne Real-Time PCR software (Applied Biosystems; 4376374). The C_t values for DOTS qPCR and fluorescence qPCR for N_0 values ranging from 1.5×10^2 to 1.5×10^5 genomic copies and for NTC are reported in Table 1. The linear relationship between the initial DNA amount and the threshold cycle for DOTS qPCR was determined to be $\log(N_0) = -0.48C_t + 6.6$, with an R^2 of 0.981. The similar linear relationship for fluorescence qPCR is $\log(N_0) = -0.24C_t + 9.4$, with an R^2 of 0.996. On average, quantification by DOTS qPCR can be done 17.53 cycles earlier than is possible using fluorescence qPCR. At a thermocycling speed of 48 s/cycle, DOTS qPCR can detect 1.5×10^5 genomic copies of bacterial DNA in 2 min 30 s and 1.5×10^2 genomic copies in 7 min 10 s, whereas a negative result can be confirmed in 11 min 31 s.

Discussion

With DOTS qPCR, real-time quantification of nucleic acids is possible for 1.5×10^5 genomic copies of bacterial DNA within 3 min 30 s (2 min 30 s for thermocycling and 1 min for sample preparation/loading). The enabling features of our novel methodology stem from interfacial effects, with the droplet stability ensured by the centrally acting interfacial tension (γ) forces. While miscellaneous tissue components are found to inhibit fluorescence qPCR (Fig. 3D), minimal sample preparation is necessary with DOT thermocycling because these inhibitory components are sequestered at the oil–water interface (Fig. 3E). The surrounding oil

environment also prevents droplet evaporation. To achieve accurate thermocycling, reaction droplets are positioned within the oil heat gradient by a feedback-controlled motor, and thermal cycle times are as short as 28 s (Fig. 4C). Furthermore, PCR amplification is detected during the early cycles because changes to the interfacial composition lead to a decrease in droplet volume. Therefore, DOTS qPCR does not require extensive thermocycling to reach the detection threshold (Fig. 5).

Inhibition relief by interfacial adsorption of contaminant proteins

An interfacial tension increase was observed upon the addition of contaminant proteins to the PCR mixture (Fig. 3B). This represents a change in the interfacial composition of the droplet due to protein diffusion to the interface (Fig. 3E). Because of their relatively high concentrations and diffusivities, the relevant blood and tissue proteins will diffuse to the interface before the *Taq* polymerases. Proteins are known to adsorb strongly at (*42*) and stabilize (*43*) the oil–water interface by a three-part process (Fig. 7B a–c)—enhanced by thermal induction of unfolding (*44*)—1) protein adsorption, 2) conformational change, and 3) aggregation (*45*). This process follows the Vroman effect (*35, 46*) and has been widely studied because of its implications in pharmaceutical and food industries. Moreover, *Taq* polymerase is thermally stable and will not become denatured during heating, whereas tissue proteins are not stable at PCR temperatures and will become denatured. Protein denaturation exposes hydrophobic residues, which increases the affinity of the protein for the oil–water interface (*45*). Without the oil–water interface, the presence of protein inhibits PCR (Fig. 3D). The interfacial adsorption described here relieves PCR inhibition and offers the potential to eliminate DNA isolation from the PCR workflow.

Association of SYBR Green with DNA to render amplicons hydrophobic

Interfacial tension is responsible for droplet-on-thermocouple stability because the centrally acting force F_γ maintains the droplet shape (Fig. 3C). The structure of SYBR Green I (SG) and its interaction with dsDNA are well-established (*47*). SG intercalates the DNA minor groove via its phenylquinilinium and benzothiazole aromatic systems, and the positively charged benzothiazole interacts electrostatically with the negatively charged phosphate groups of dsDNA. In addition, the dsDNA/SG complex is stabilized by the positively charged dimethylaminopropyl group, which extends along the minor groove for 3–4 base pairs. The overall size of the SG binding site is equal to 3.4 bp or 11.5 Å. Unbound SG is an amphiphilic molecule containing positively charged propyl groups as well as aromatic rings. Therefore, when SG intercalates dsDNA, the positively charged SG partially neutralizes the negatively charged phosphate backbone of dsDNA. When dsDNA is amplified, the dsDNA/SG complex is formed, which has high affinity for the oil–water interface. As the dsDNA/SG complex concentration increases, the interfacial tension decreases markedly (Fig. 6C).

The role of the dsDNA/SG complex in DOTS qPCR

Before PCR amplification, high-motility proteins with low interface affinity adsorb reversibly and are subsequently displaced by proteins that have high concentration, higher affinity for the interface, and lower motility; this is known as the Vroman effect (*35, 42*). In DOT thermocycling, the dsDNA concentration is exponentially increased by PCR, and the relatively hydrophobic dsDNA/SG complex accumulates. Adsorption of the dsDNA/SG complex at the interface causes proteins to desorb, dramatically decreasing the interfacial tension. As the interfacial tension decreases, the entropy penalty of interaction between oil and water decreases

as well (Fig. 7B). Since higher surface area to volume ratios are permitted when the surface energy is decreased, droplets with a volume of 0.5–4.2 fL separate from the droplet-on-thermocouple and become emulsified in the oil phase (Fig. 7A).

As shown in Figure 5, the decrease in interfacial tension, which leads to a decrease in the droplet-on-thermocouple volume, is dependent on N_0 of the reaction, because N_t is reached at earlier cycles for reactions with higher N_0. There is a log-linear relationship between N_0 and the threshold cycle *(C_t):* $\log(N_0) = -0.48C_t + 6.6$. This relationship can be used to quantify unknown N_0, in the range of 1.5×10^2 to 1.5×10^5 copies of bacterial genomic DNA. Typical clinical concentrations for IE range from 10^7–10^9 CFU/g of vegetated heart valve tissue (*17, 20, 40*) with inocula ranging from 10^4–10^9 CFU (*40*). The quantitative range of DOTS qPCR is a good match for this clinical situation, considering the sample preparation method, sample size, and the limit of detection of 1.5×10^2 genomic copies.

Comparison of interfacial tension detection with fluorescence detection

Figure 6 shows that interfacial tension can be used to detect PCR amplification at earlier thermal cycles than can be achieved with fluorescence or gel electrophoresis. PCR amplification is described by Eq. 1 (*48, 49*), where E is the reaction efficiency, C_n is the number of cycles, N_0 is the initial number of amplicons, and N_n is the number of amplicons after n cycles.

$$N_n = N_0(E+1)^{C_n} \tag{1}$$

In the case of fluorescence detection, a threshold (F_t) can be chosen to calculate the corresponding threshold cycle (C_t). The number of amplicons at C_t (N_t) is the same for any N_0. We therefore use N_t to compare the DOTS qPCR and fluorescence qPCR detection techniques. The standard curves for both the methods are presented in Figure 8. For both the methods, N_t is calculated from the intercept in the log-linear equation (Eq. 2) of the standard curve (*48, 49*).

$$\log N_0 = -C_t \log(E+1) + \log N_t \tag{2}$$

SG fluorescence is increased by 1000 times upon forming a complex with dsDNA (*47*), but this fluorescence signal is not detectable by fluorescence qPCR until 1.28×10^{10} amplicons are present. In contrast, the detection threshold in DOTS qPCR is reached at 3.96×10^6 copies (Fig. 8A).

For interfacial tension detection, we may assign N_t a physical meaning by using the Langmuir adsorption isotherm equation (Eq. 3), where θ is the fractional coverage ($\theta = \Gamma/\Gamma_{max}$), Γ is the adsorbed amount, Γ_{max} is the amount adsorbed at saturation, C is the equilibrium concentration, and K_{ads} is the equilibrium constant for adsorption/desorption.

$$\theta = \frac{K_{ads}C}{1+K_{ads}C} \tag{3}$$

The Langmuir adsorption isotherm equation describes the filling of available surface sites as a function of concentration. As the equilibrium concentration increases with each thermal cycle, a similar saturation effect is seen in the interfacial tension with respect to the cycle number (Fig.

6C). To apply this interfacial adsorption to interfacial tension, we must consider the energy associated with molecular adsorption. For this purpose, we turn to the Gibbs adsorption isotherm at constant temperature (Eq. 4), where γ is the interfacial tension, Γ is the adsorbed amount, and μ is the chemical potential.

$$d\gamma = -\sum \Gamma_i d\mu_i \tag{4}$$

From the Gibbs adsorption isotherm, we can see that the interfacial tension (γ) is sensitive to the adsorbed amount (Γ) and the change in the interfacial tension ($d\gamma$) will be zero when Γ_{max} is reached. The Langmuir and Gibbs adsorption isotherms allow us to define N_t for DOTS qPCR as the amount of DNA amplicons necessary to cause a sufficiently large decrease in interfacial tension that results in a fractional volume loss of 4.8%.

Impact of DOTS qPCR on medical diagnostics and biological research

The reduction in interfacial tension upon DNA amplification in the presence of SG causes a fractional loss of volume because femtoliter-sized water droplets become emulsified in the oil phase. Moreover, the logarithm of N_0 scales linearly with the fractional thermal cycle at which the percent decrease in droplet height reaches the 4.8% threshold. This relationship can be used for quantification in a manner identical to fluorescence qPCR but at a lower threshold cycle (Fig. 8). Quantification by DOTS qPCR can be accomplished in less than 4 thermal cycles and takes 2 min 30 s (3 min 30 s including sample preparation/loading). Fluorescence qPCR systems require excitation and emission band-pass filters, a dichroic mirror, an expensive light source (tungsten-halogen lamp or argon ion laser), a sensitive detector (typically photomultiplier tube), a completely dark environment, and an external computer. In contrast, the DOTS qPCR detection system is composed of a single lens and a smartphone under ambient lighting. Furthermore, disposability is a necessary feature of medical diagnostics. All components of the DOTS qPCR device that come into contact with the sample—the semicircular channel, motor arm, thermocouple, heating element, and silicone oil—are inexpensive (less than $20 for all components) and disposable.

PCR is widespread in biological research and medical diagnostics. While all users could benefit from the increased assay speed, our methodology could have an immediate impact on patients for whom time is truly of the essence. Therefore, we have demonstrated DOTS qPCR to diagnose tissue infection, which could result in informed clinical decision-making and a decreased loss of life. We anticipate extending this technology to biological research applications such as analyses from single cells, single nuclei, and single molecules (*50*). These applications require greater than 40 thermal cycles to reach the fluorescence detection threshold, and excessive thermocycling can decrease specificity by amplifying low-level background contamination and non-specific targets. Therefore, low threshold cycle detection would improve the analysis of these small samples.

Our work is the first reported use of interfacial effects to detect PCR amplification. This is an important technical advancement, not only because of the simplicity of the thermocycler and detection apparatus, but also because it enables detection at low cycle numbers. Because of its extremely high speed, DOTS qPCR can be used unlike any existing technique for tissue infection diagnosis—in the clinic or operating room before initial prescription of therapy. With DOTS

qPCR, infection diagnosis will be timely and surveillance of antibiotic resistance will be convenient and widespread.

Materials and Methods

Polymerase chain reaction (PCR)

There are two different thermocycling modalities and two different real-time detection modalities that are reported in this work. The thermocycling modalities are termed *conventional thermocycling* and *droplet-on-thermocouple (DOT) thermocycling*. The real-time PCR (qPCR) modalities are termed *fluorescence qPCR* and *droplet-on-thermocouple silhouette (DOTS) qPCR*. There were three different target samples used. Vancomycin-sensitive *Enterococcus faecalis* (VSE, ATCC© 33186™) and vancomycin-resistant *Enterococcus faecium* (VRE, *Enterococcus* ATCC© 700221™) were propagated according to the procedure outlined in the ATCC product sheet to 10^8 CFU/mL, pelleted by centrifugation at 6000 × *g* (where *g* is the acceleration due to gravity) for 10 min, re-suspended in 100 μL molecular grade water, and heat-killed at 95°C for 15 min. Purified *Klebsiella pneumoniae* strain Z026 genomic DNA was purchased from ZeptoMetrix.

Three primer sets were used. The plasmid-mediated antibiotic resistance gene *vanA* was targeted by the *vanA* primers (*13*): F: 5'-TCT GCA ATA GAG ATA GCC GC-3' and R: 5'-GGA GTA GCT ATC CCA GCA TT-3'. The *vanA* amplicon is 377 bp in length. The amplicon length and primer pairing were confirmed by mapping to the VRE *vanA* gene (accession number AB247327) (*51*). The 16S rRNA gene was targeted at the hypervariable regions V3 and V1–V2. The V3 primer sequences are F: 5'-ACT CCT ACG GGA GGC AGC AG-3' and R: 5'-ATT ACC GCG GCT GCT GG-3', yielding an amplicon length of 196 bp (*52*). The V1–V2 primer sequences are F: 5'-AGA GTT TGA TCM TGG CTC AG-3' and R: 5'-CYI ACT GCT GCC TCC CGT AG-3' for an amplicon length of 353 bp.

The PCR recipe varies by modality, but the standard PCR recipe was used for most experiments and should be assumed unless otherwise noted. The standard PCR cocktail is composed of the following components: PCR master mix [GoTaq Green Master Mix 2x (Promega; M7122), GoTaq Colorless Master Mix 2x (Promega; M7132) or Fast SYBR Green Master Mix 2x (Applied Biosystems; 4385612)], forward and reverse primers (10 μM), target, and nuclease-free water; the components are in the proportion 5:1:1:3, respectively. The target proportion is increased for the heart valve tissue biopsy by reducing the water content. The real-time detection modalities (fluorescence qPCR and DOTS qPCR) use modified PCR cocktails.

Design and fabrication of DOTS qPCR device

The mechanical aspects of the device were designed using the computer-aided design software SolidWorks, and the custom parts were 3D printed out of acrylonitrile butadiene styrene (ABS) polymer using Dimension uPrint SE. Nickel-chromium heating wire (Omega; NI60-010-200) with a resistance per length of 22.15 Ω/m was wound in a serpentine manner and pressed between two 25 × 19 mm sections of double-sided solvent-resistant tape (McMaster-Carr; 75955A672). The tape ensures that the wire does not make self-contact. The final resistance of the heater was 10 Ω. Single-sided adhesive Teflon tape (McMaster-Carr; 8711K22) was applied to the top surface of the heater assembly to minimize fouling. A heater was bent into each end of the semicircular channel and secured with quick-cure glue (Gorilla Glue; 39038). The ends of the

heater wire were connected to the PID controller via copper wire. A 36-gauge type K thermocouple (Omega; 5TC-TT-K-36-36) was mounted 5 mm above the surface of both heaters to serve as feedback control. The PID controller was custom designed to regulate the 7.5 V, 0.75 A heater power supply. The channel was filled with 8 mL silicone oil (Santa Cruz Biotechnology; sc-215854A) before every sample, and the channel was washed extensively with sodium hypochlorite, ethanol, and deionized water between samples. For real-world use, the following components of the device are disposable and meant for one-time use: the semicircular channel, motor arm, thermocouple, heating element, and silicone oil. The set temperatures at the heat gradient extremes (101°C and 50°C) were equilibrated to steady state within 10 min of commencing temperature ramping. A heat gradient was established between the temperature extremes and verified by a thermocouple traveling at 17.6°/s around the semicircular channel. All temperatures between the two set points were represented.

A thermocouple for droplet suspension was bent into a loop with a diameter of 3 mm, and the thermocouple junction was bent downward below the center of the loop. The thermocouple loop was mounted on the motor arm such that it was completely submerged below the surface of the oil. The thermocouple loop provides droplet temperature feedback and records the droplet temperatures. Each thermocouple was used only for a single sample, after which it was discarded to avoid contamination and non-specific amplification. A miniature motor (NMB Technologies; PG15S-D20-HHB9) with 0.176° step angle was fixed concentric to the semicircular channel. The motor was powered by the microcontroller (Arduino Mega) power supply and controlled by a motor controller circuit assembly (Sparkfun Electronics; Easydriver). The zero position corresponds to the site of the viewing window and was calibrated using an IR photogate.

An optically transparent fused silica window (Edmund Optics; #45-309) separates the oil from the lens of the smartphone camera. This window creates a view into the channel at the 70°C region of the heat gradient. An adjustable lens tube (ThorLabs; SM05V05) containing an N-BK7 plano-convex lens (ThorLabs; LA1560) focuses the image on the smartphone camera (Apple iPhone 4) at a focal point 22.7 mm from the back planar surface of the lens. The lens tube was connected to the smartphone via a custom designed smartphone housing that aligns the lens with the smartphone camera.

Conventional thermocycling

Conventional thermocycling was conducted using the MJ Research Minicycler. One cycle consists of the following three phases: denaturation for 30 s at 95°C, annealing for 30 s at 58°C, and extension for 40 s at 72°C. In order to analyze samples at increments of 5 cycles for 0–30 cycles, seven replicate PCR cocktails were prepared. The zero-cycle sample was not thermocycled, and the remaining six samples were thermocycled for 5 cycles at a time. One sample was removed from the thermocycler every 5 cycles and stored in a 4°C refrigerator. For samples that were continuously cycled for 30 cycles, a 3 min initial denaturation step at 95°C and a 10 min final extension step at 72°C were added.

Droplet-on-thermocouple (DOT) thermocycling

Using a micropipette, 5–10 μL of PCR cocktail were dispensed onto the thermocouple loop such that the droplet was completely submerged in the heated oil. The droplet was dispensed with the motor arm positioned at the low-temperature region, to avoid non-specific extension before initial denaturation and annealing. PCR protocols were programmed for automatic device

operation, and the device could be run in multiple modes. The droplet position can be determined either by predefined temperature mapping or by real-time temperature feedback. For temperature feedback, the thermocouples mounted on the motor arm measure the oil and droplet temperatures. The device is reprogrammable to allow for different PCR protocols. Under typical thermocycling, the droplet is never held stationary so that the continuous movement enhances heat transfer by convection.

Gel electrophoresis

The PCR products were analyzed by gel electrophoresis. For amplicons between 100 bp and 500 bp, 3% w/v agarose gel (Sigma; A0169) in 1x tris-acetate-EDTA (TAE) buffer (Invitrogen; 24710-030) was used. A 1 kb Plus DNA ladder (Invitrogen; 10787) was used as the length standard, and 4 μL of sample were added to each lane. An electrophoresis power supply (Fischer Scientific; FB200) provided a potential of 120 V for 40 min. The gels were stained with ethidium bromide (Sigma; E1510), washed with 1x TAE, and imaged under UV irradiation. The images were analyzed with ImageJ software (U.S. National Institutes of Health).

Real-time PCR on a fluorescence qPCR instrument and standard curve construction

A real-time PCR (qPCR) standard curve was constructed on the StepOne Real-Time PCR System (Applied Biosystems; 4376374). The PCR cocktail contained 25 μL of Fast SYBR Green Master Mix (Applied Biosystems; 4385612), 1 μL of forward and reverse primers (10 μM each), 1 μL of target DNA, and 23 μL of nuclease-free water, for a total volume of 50 μL. The thermocycler was programmed for 40 cycles of 95°C for denaturation and 60°C for annealing, followed by the dissociation protocol. PCRs were run in triplicate for each initial target amount (N_0) using 10-fold serial dilutions of the *Klebsiella pneumoniae* strain Z026 genomic DNA from 1.5×10^2 to 1.5×10^5 genomic copies. The number of genomic copies was estimated using a genomic mass of 5 fg. A fluorescence threshold ($F_t = 1.0$) was chosen within the exponential phase of amplification, and the C_t values were calculated using the StepOne software. The logarithm of N_0 was plotted against the average C_t value for each N_0, and a trend line was established for this plot using linear regression analysis: $\log(N_0) = -0.278\ C_t + 12.1$. The slope [$-\log(E+1)$] was used to calculate the slope-derived efficiency ($E_S = 89.5\%$), and the y-intercept [$\log(N_t)$] was used to determine the number of amplicons at F_t ($N_t = 1.15 \times 10^{12}$ copies).

Porcine model for infective endocarditis

A porcine heart was procured from the University of Arizona College of Agriculture and Life Sciences Food Products and Safety Laboratory (USDA FSIS; M966-P19049-V966). The aortic, mitral, and tricuspid valves were excised from the heart under sterile conditions, and 6 mm circular sections were cut using a skin biopsy punch. To ensure sterility, the valve sections were incubated overnight on a 12-well tissue culture plate in antibiotic-containing M199 tissue culture media at 4°C. For cryopreservation, the valve sections were transferred to M199 tissue culture media with 10% v/v glycerol. The cryovials were transferred into a Nalgene 1°C freezing container, and this was placed in a –40°C freezer overnight. After freezing, the cryovials were transferred to a freezer box. To prepare the tissue samples for PCR, the valve sections were thawed, the tissue culture media was removed, and the tissue was washed twice with nuclease-free water. The sections were inoculated with 10 μL of vancomycin-resistant *Enterococcus faecium* (VRE, ATCC© 700221™) in nuclease-free water at 10^9 CFU/mL, and then 10 μL of nuclease-free water was added. Debridement was simulated by grinding the inoculated tissue

with a micro-mortar and -pestle (BioMasher II) for 1 min. The liquid phase of the ground tissue was used as the PCR target without further purification. To evaluate the inhibition effect of the tissue contamination, the Applied Biosystems ABI Prism 7000 Sequence Detection System was used, and the C_t values were calculated with an F_t of 1.0.

Protein quantification

The Bradford assay (Quick Start Bradford Protein Assay, Bio-Rad) was used to determine the protein content of the tissue sample after grinding. Standard curves were created for the assay using bovine serum albumin (BSA) and gamma globulin. The protein content of the tissue sample was estimated as a range using the BSA standard curve as the lower limit and the gamma globulin standard curve as the upper limit. BSA has a higher affinity for the Bradford dye than gamma globulin.

Interfacial tension (γ) measurement

The interfacial tension was measured by the pendant droplet method on an FTÅ 200 contact angle and interfacial tension analyzer. Pendant droplets were extruded from an 18-gauge blunt needle tip (Jensen Global; JG18) with an inside diameter of 0.9652 mm, and interfacial tension measurements were made at droplet equilibration at 2, 4, and 6 min after extrusion. The average interfacial tension, along with the standard error, was plotted.

Visualization of emulsified femtoliter droplets

The miscibilities of the thermocycled PCR cocktails were characterized by light microscopy to determine the volume of emulsified droplets of the PCR mixture in the oil phase. A 40 μL PCR cocktail containing 4 ng of *K. pneumoniae* genomic DNA and Fast SYBR Green Master Mix was conventionally thermocycled for the amplification of the 16S rRNA V3 amplicon with a 40 μL silicone oil overlay. Following thermocycling, the oil and water were vortex mixed and allowed to settle. Then, 5 μL of the oil phase was pipetted onto a glass microscope slide and covered with a coverslip to be visualized by light microscopy.

Droplet-on-thermocouple silhouette real-time PCR (DOTS qPCR)

Real-time detection of PCR amplification was achieved by analyzing the droplet-on-thermocouple silhouette during thermocycling. A special PCR cocktail was formulated to aid in the visualization of the droplet-on-thermocouple silhouette. This cocktail contains Fast SYBR Green Master Mix, GoTaq Green Master Mix, forward and reverse primers (10 μM), target, and nuclease-free water in the proportion 5:1:1:1:2. For 0–15 cycles, the droplet was positioned in front of the viewing window, which is located at the 70°C region of the heat gradient. The image of the droplet was captured by a smartphone camera (Apple iPhone 4) every 5 cycles, and the droplet height at the center was determined by analysis with the ImageJ software. The percent decrease in droplet height with respect to the droplet height at cycle zero was plotted against the cycle number.

Supplementary Materials

Fig. S1. Gel electrophoresis of PCR amplification at different cycle numbers. (**A**) Gel electropherogram of 16S rRNA V3 amplicon (196 bp) amplified from 75 pg *K. pneumoniae*

genomic DNA (1.5×10^4 genomic copies), conventionally thermocycled in increments of five cycles with SYBR Green I (SG). (**B**) Gel electropherogram of 16S rRNA V3 amplicon (196 bp) amplified from 75 pg *K. pneumoniae* genomic DNA (1.5×10^4 genomic copies) without SG. (**C**) Gel electropherogram of a no template control sample thermocycled with SG.

Movie S1. DOTS qPCR device operation. This movie demonstrates DOTS qPCR operation. The motor arm with the mounted thermocouple loop submerged beneath the surface of the oil is positioned at the low-temperature region of the heat gradient. A 5–10 µL droplet of PCR cocktail is positioned on the thermocouple loop using a pipette, and the thermocycling program is initiated.

Movie S2. Droplet imaging by smartphone. Before the first thermal cycle, the droplet is positioned in front of the viewing window, and an image of the droplet-on-thermocouple silhouette at cycle zero is captured by the smartphone camera. The droplet then moves to the high-temperature region for the initial denaturation.

Movie S3. Close-up view of convective heating. Close-up view of the droplet being cooled at the low-temperature region of the heat gradient, for the annealing phase of the reaction, after initial denaturation.

Movie S4. Whole-device view of a complete thermal cycle. This movie shows a whole-device view of the droplet going through a complete thermal cycle. It moves from the low-temperature region for annealing, then to the 72°C region for extension, and finally to the high-temperature region for denaturation. Thermocycling repeats in this fashion until the fifth thermal cycle, when another image of the droplet-on-thermocouple silhouette is taken for analysis and quantification of the initial target concentration.

References

1. M. P. Jevons, “Celbenin”-resistant staphylococci. *Brit. Med. J.* **1**, 124 –126. (1961)

2. D. Hughes, Exploiting genomics, genetics and chemistry to combat antibiotic resistance. *Nat. Rev. Genet.* **4**, 432–41 (2003).

3. L. M. Weigel, D. B. Clewell, S. R. Gill, N. C. Clark, L. K. McDougal, S. E. Flannagan, J. F. Kolonay, J. Shetty, G. E. Killgore, F. C. Tenover, Genetic analysis of a high-level vancomycin-resistant isolate of *Staphylococcus aureus*. *Science* **302**, 1569–71 (2003).

4. D. P. Levine, Vancomycin: a history. *Clin. Infect. Dis.* **42** Suppl 1, S5–12 (2006).

5. A. H. C. Uttley, C. H. Collins, J. Naidoo, R. C. George, Vancomycin-resistant Enterococci. *The Lancet* 57–58 (1988).

6. P. Courvalin, Vancomycin resistance in gram-positive cocci. *Clin. Infect. Dis.* **42** Suppl 1, S25–34 (2006).

7. B. E. Murray, Vancomycin-resistant enterococcal infections. *New Engl. J. Med.* **342**, 710–21 (2000).

8. B. Périchon, P. Courvalin, VanA-type vancomycin-resistant *Staphylococcus aureus*. *Antimicrob. Agents Chemother.* **53**, 4580–7 (2009).

9. W. C. Noble, Z. Virani, R. G. Cree, Co-transfer of vancomycin and other resistance genes from *Enterococcus faecalis* NCTC 12201 to *Staphylococcus aureus*. *FEMS Microbiol. Lett.* **72**, 195–8 (1992).

10. V. N. Kos, C. A. Desjardins, A. Griggs, Commonly associated with comparative genomics of vancomycin-resistant *Staphylococcus* associated with methicillin-resistant *S. aureus* hospital-acquired. *MBio* **3**, e00112–12 (2012).

11. G. R. Pupp, W. J. Brown, D. Cardo, S. K. Fridkin, Infection with vancomycin-resistant. *New Engl. J. Med.* **348**, 1342–7 (2013).

12. *Antibiotic Resistance Threats in the United States*. (U.S. Centers for Disease Control and Prevention, 2013) [http://www.cdc.gov/drugresistance/threat-report-2013].

13. F. F. Syed, B. C. Millar, B. D. Prendergast. Molecular technology in context: a current review of diagnosis and management of infective endocarditis. *Prog. Cardiovasc. Dis.* **50**, 181–97 (2007).

14. H. Volkmann, T. Schwartz, P. Bischoff, S. Kirchen, U. Obst, Detection of clinically relevant antibiotic-resistance genes in municipal wastewater using real-time PCR (TaqMan). *J. Microbiol. Meth.* **56**, 277–86 (2004).

15. C. L. Brinkman, P. Vergidis, J. R. Uhl, B. S. Pritt, F. R. Cockerill, J. M. Steckelberg, L. M. Baddour, J. J. Maleszewski, W. D. Edwards, R. Sampath, R. Patel, PCR-electrospray ionization mass spectrometry for direct detection of pathogens and antimicrobial resistance from heart valves in patients with infective endocarditis. *J. Clin. Microbiol.* **51**, 2040–6 (2013).

16. I.-G. Bae, J. J. Federspiel, J. M. Miró, C. W. Woods, L. Park, M. J. Rybak, T. H. Rude, S. Bradley, S. Bukovski, C. G. de la Maria, S. S. Kanj, T. M. Korman, F. Marco, D. R. Murdoch, P. Plesiat, M. Rodriguez-Creixems, P. Reinbott, L. Steed, P. Tattevin, M.-F. Tripodi, K. L. Newton, G. R. Corey, V. G. Fowler. Heterogeneous vancomycin-intermediate susceptibility phenotype in bloodstream methicillin-resistant *Staphylococcus aureus* isolates from an international cohort of patients with infective endocarditis: prevalence, genotype, and clinical significance. *J. Infect. Dis.* **200**, 1355–66 (2009).

17. L. M. Baddour, W. R. Wilson, A. S. Bayer, V. G. Fowler, A. F. Bolger, M. E. Levison, P. Ferrieri, M. A. Gerber, L. Y. Tani, M. H. Gewitz, D. C. Tong, J. M. Steckelberg, R. S. Baltimore, S. T. Shulman, J. C. Burns, D. A. Falace, J. W. Newburger, T. J. Pallasch, M. Takahashi, K. A. Taubert, Infective Endocarditis. *Circulation* **111**, 3167–84 (2005).

18. A. S. Bayer, A. F. Bolger, K. A. Taubert, W. Wilson, J. Steckelberg, A. W. Karchmer, M. Levison, H. F. Chambers, A. S. Dajani, M. H. Gewitz, J. W. Newburger, M. A. Gerber, S. T. Shulman, T. J. Pallasch, T. W. Gage, P. Ferrieri, Diagnosis and management of infective endocarditis and its complications. *Circulation* **98**, 2936–48 (1998).

19. D. M. Wolk, W. M. Dunne New technologies in clinical microbiology. *J. Clin. Microbiol.* **49**, S62–7 (2011).

20. M. Marín, P. Muñoz, M. Sánchez, M. del Rosal, L. Alcalá, M. Rodríquez-Créixems, E. Bouza, Molecular diagnosis of infective endocarditis by real-time broad-range polymerase chain reaction (PCR) and sequencing directly from heart valve tissue. *Medicine (Baltimore)* **86**, 195–202 (2007).

21. V. Gauduchon, L. Chalabreysse, J. Etienne, M. Célard, Y. Benito, H. Lepidi, F. Thivolet-Béjui, F. Vandenesch, Molecular diagnosis of infective endocarditis by PCR amplification and direct sequencing of DNA from valve. *J. Clin. Microbiol.* **41**, 763-6 (2003).

22. C. Breitkopf, D. Hammel, H. H. Scheld, G. Peters, K. Becker, Impact of a molecular approach to improve the microbiological diagnosis of infective heart valve endocarditis. *Circulation* **111**, 1415–21 (2005).

23. M. Vondracek, U. Sartipy, E. Aufwerber, I. Julander, D. Lindblom, K. Westling, 16S rDNA sequencing of valve tissue improves microbiological diagnosis in surgically treated patients with infective endocarditis. *J. Infect.* **62**, 472–8 (2011).

24. B. E. Giessel, C. J. Koenig, R. L. Blake, Management of bacterial endocarditis. *Am. Fam. Physician* **61**, 1725–32 (2000).

25. P. M. da Costa, L. Loureiro, A. J. F. Matos, Transfer of multidrug-resistant bacteria between intermingled ecological niches: the interface between humans, animals and the environment. *Int. J. Environ. Res. Public Health* **10**, 278–94 (2013).

26. L. E. Lehmann, K.-P. Hunfeld, T. Emrich, G. Haberhausen, H. Wissing, A. Hoeft, F. Stüber, A multiplex real-time PCR assay for rapid detection and differentiation of 25 bacterial and fungal pathogens from whole blood samples. *Med. Microbiol. Immun.* **197**, 313–24 (2008).

27. P.P. Banada, S. Chakravorty, D. Shah, M. Burday, F. M. Mazzella, D. Alland, Highly sensitive detection of *Staphylococcus aureus* directly from patient blood. *PLoS ONE* **7**, e31126 (2012).

28. C. S. Price, S. E. Kon, S. Metzger, Rapid antibiotic susceptibility phenotypic characterization of *Staphylococcus aureus* using automated microscopy of small numbers of cells. *J. Microbiol. Meth.* **98**, 50–8 (2014).

29. Y.-H. Chang, G.-B. Lee, F.-C. Huang, Y.-Y. Chen, J.-L. Lin, Integrated polymerase chain reaction chips utilizing digital microfluidics. *Biomed. Microdev.* **8**, 215–25 (2006).

30. J.-Y. Yoon, B. Kim, Lab-on-a-chip pathogen sensors for food safety. *Sensors* **12**, 10713–41 (2012).

31. R. Prakash, D. P. Papageorgiou, A. G. Papathanasiou, K. V. I. S. Kaler, Dielectrophoretic liquid actuation on nano-textured super hydrophobic surfaces. *Sens. Actuat. B* **182**, 351–361 (2013).

32. D. J. You, P. L. Tran, H.-J. Kwon, D. Patel, J.-Y. Yoon, Very quick reverse transcription polymerase chain reaction for detecting 2009 H1N1 influenza A using wire-guide droplet manipulations. *Faraday Discuss.* **149**, 159-70 (2011).

33. O. N. Chuang-Smith, C. L. Wells, M. J. Henry-Stanley, G. M. Dunny, Acceleration of *Enterococcus faecalis* biofilm formation by aggregation substance expression in an ex vivo model of cardiac valve colonization. *PLoS ONE* **5**, e15798 (2010).

34. S. Akhtar, K. M. Meek, V. James, Immunolocalization of elastin, collagen type I and type III, fibronectin, and vitronectin in extracellular matrix components of normal and myxomatous mitral heart valve chordae tendineae. *Cardiovasc. Pathol.* **8**, 203–11 (1999).

35. K. C. Dee, D. A. Puleo, R. Bizios, An introduction to tissue-biomaterial interactions, John Wiley & Sons: Hoboken, 2002, pp. 37-52.

36. P. Knox, S. Crooks, C. S. Rimmer, Role of fibronectin in the migration of fibroblasts into plasma clots. *J. Cell Biol.* **102**, 2318–23 (1986).

37. F. H. Silver, R. L. Trelstad. Type I collagen in solution. *J. Biol. Chem.* **255**, 9427–33 (1980).

38. P. Toonkool, D. G. Regan, P. W. Kuchel, M. B. Morris, A. S. Weiss, Thermodynamic and hydrodynamic properties of human tropoelastin: analytical ultracentrifuge and pulsed field-gradient spin-echo NMR studies. *J. Biol. Chem.* **276**, 28042–50 (2001).

39. Z. Bu, R. Biehl, M. Monkenbusch, D. Richter, D. J. E. Callaway. Coupled protein domain motion in Taq polymerase revealed by neutron spin-echo spectroscopy. *Proc. Natl. Acad. Sci. USA* **102**, 17646–51 (2005).

40. L. M. Baddour, G. D. Christensen, A. L. Bisno, Bacterial concentration correlations in experimental endocarditis caused by *Staphylococcus epidermidis*. *J. Clin. Microbiol.* **25**, 207–10 (1987).

41. D. K. Harshman, R. Reyes, T. S. Park, D. J. You, J.-Y. Song, J.-Y. Yoon, Enhanced nucleic acid amplification with blood in situ by wire-guided droplet manipulation (WDM). *Biosens. Bioelectron.* **53,** 167–74 (2014).

42. N. Dixit, K. M. Maloney, D. S. Kalonia, Protein-silicone oil interactions: comparative effect of nonionic surfactants on the interfacial behavior of a fusion protein. *Pharm. Res.* **30**, 1848–59 (2013).

43. D. B. Ludwig, J. F. Carpenter, J.-B. Hamel, T. W. Randolph, Protein adsorption and excipient effects on kinetic stability of silicone oil emulsions. *J. Pharm. Sci.* **99**, 1721–33 (2010).

44. A. Gerhardt, K. Bonam, J. S. Bee, J. F. Carpenter, T. W. Randolph, Ionic strength affects tertiary structure and aggregation propensity of a monoclonal antibody adsorbed to silicone oil – water interfaces. *J. Pharm. Sci.* **102**, 429–40 (2013).

45. C. J. Beverung, C. J. Radke, H. W. Blanch, Protein adsorption at the oil/water interface: characterization of adsorption kinetics by dynamic interfacial tension measurements. *Biophys. Chem.* **81**, 59–80 (1999).

46. J.-H. Kim, J.-Y. Yoon, Protein adsorption on polymer particles. In: *Encyclopedia of Surface and Colloid Science*, Marcel Dekker: New York, 2002, pp. 4373–81.

47. A. I. Dragan, R. Pavlovic, J. B. McGivney, J. R. Casas-Finet, E. S. Bishop, R. J. Strouse, M. A. Schenerman, C. D. Geddes, SYBR Green I: fluorescence properties and interaction with DNA. *J. Fluoresc.* **22**, 1189–99 (2012).

48. R. G. Rutledge, C. Côté, Mathematics of quantitative kinetic PCR and the application of standard curves. *Nucleic Acids Res.* **31**, e93 (2003).

49. R. Higuchi, C. Fockler, G. Dollinger, R. Watson, Kinetic PCR analysis: real-time monitoring of DNA amplification reactions. *Biotechnology* **11**, 1026–30 (1993).

50. R. V. Grindberg, J. L. Yee-Greenbaum, M. J. McConnell, M. Novotny, A. L. O'Shaughnessy, G. M. Lambert, M. J. Araúzo-Bravo, J. Lee, M. Fishman, G. E. Robbins, X. Lin, P. Venepally, J. H. Badger, D. W. Galbraith, F. H. Gage, R.S. Lasken. RNA-sequencing from single nuclei. *Proc. Natl. Acad. Sci. USA* **110**, 19802–7 (2013).

51. S.-K. Lim, K. Tanimoto, H. Tomita, Y. Ike, Pheromone-responsive conjugative vancomycin resistance plasmids in *Enterococcus faecalis* isolates from humans and chicken feces. *Appl. Environ. Microbiol.* **72**, 6544–53 (2006).

52. A. Sundquist, S. Bigdeli, R. Jalili, M. L. Druzin, S. Waller, K. M. Pullen, Y. Y. El-Sayed, M. M. Taslimi, S. Batzoglou, M. Ronaghi, Bacterial flora-typing with targeted, chip-based Pyrosequencing. *BMC Microbiol.* **7**, 108 (2007).

Acknowledgements

General

This work was supported by the Cardiovascular Biomedical Engineering Training Grant from the U.S. National Institutes of Health (NIH grant T32HL007955) and the U.S. National Science Foundation grant (NSF grant CBET-1511093). We thank Prof. David G. Armstrong and Dr. Nicholas A. Giovinco for discussions on the use of technology in the clinic and operating room, Dr. Scott V. Angus and Dr. Tu San Park for helpful discussions, Dr. David W. Galbraith for valuable discussions and manuscript edits, Mrs. Candice Parker for support with fluorescence qPCR experiments, and Prof. Denise J. Roe for statistical assistance. We are also grateful to the Genomics Core at the University of Arizona Cancer Center, which is supported by the Southwest Environmental Health Center (NIH NIEHS grant ES06694) and the Arizona Cancer Center (NIH grant CA23074), for access to the ABI 7000 for fluorescence qPCR experiments.

Author contributions

D.K.H. and J.Y.Y. conceived of the project; D.K.H. designed, fabricated, and tested the DOTS qPCR device; G.S.W. directed the fluorescence qPCR experiments and supported the

fluorescence qPCR data analysis; D.K.H. and B.M.R. performed the experiments; J.E.M. supported the antibiotic resistance experiments and microbial culture; D.K.H. and J.Y.Y. analyzed the data; D.K.H. wrote the manuscript with edits from all authors.

Competing financial interests

The authors declare that they have no competing interests.

Figures and Tables

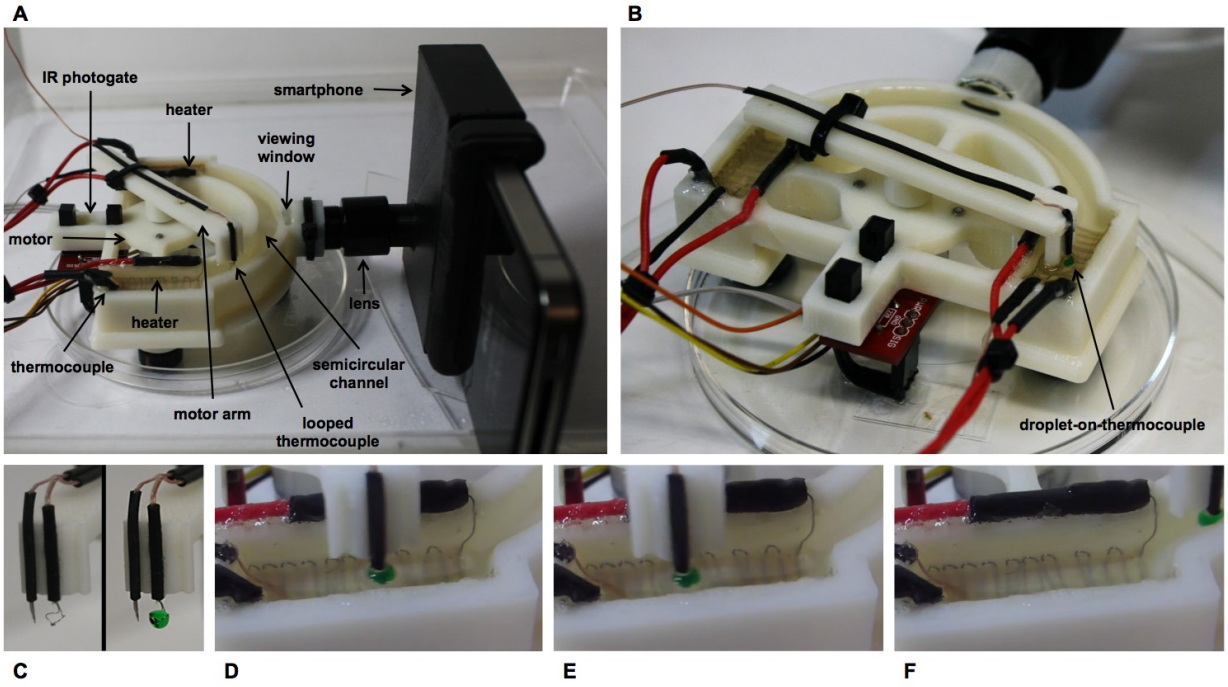

Fig. 1. Droplet-on-thermocouple silhouette real-time PCR device. (**A**) The droplet-on-thermocouple silhouette real-time PCR (DOTS qPCR) device showing all components: semicircular channel with PID-controlled heaters positioned at both ends, feedback thermocouples mounted 5 mm above the heater surface, motor arm with looped thermocouple mounted for droplet suspension in heated oil, viewing window at the center of the channel, and lens tube to focus and magnify the droplet image onto the smartphone camera. All components are disposable after one use except for the motor, lens tube, and smartphone. (**B**) Alternate view showing the droplet-on-thermocouple moving to the low temperature side of the heat gradient. (**C**) Two thermocouples mounted on the motor arm. The straight thermocouple is used for oil temperature measurement, and the looped thermocouple holds the droplet and measures the droplet temperature. (**D, E**) Still images of the submerged droplet moving back and forth continuously at the low-temperature region. The thermocouple junction is inside the droplet to monitor the reaction temperature. Droplet temperature feedback is used by the motor program to accurately position the droplet in the heat gradient. The still images are screen captures from the supplementary video showing device operation (Movie S3). (**F**) Still image of the droplet moving away from the low-temperature region after completing annealing, to be positioned at a warmer region corresponding to the optimum temperature for *Taq* polymerase extension of the PCR amplicon.

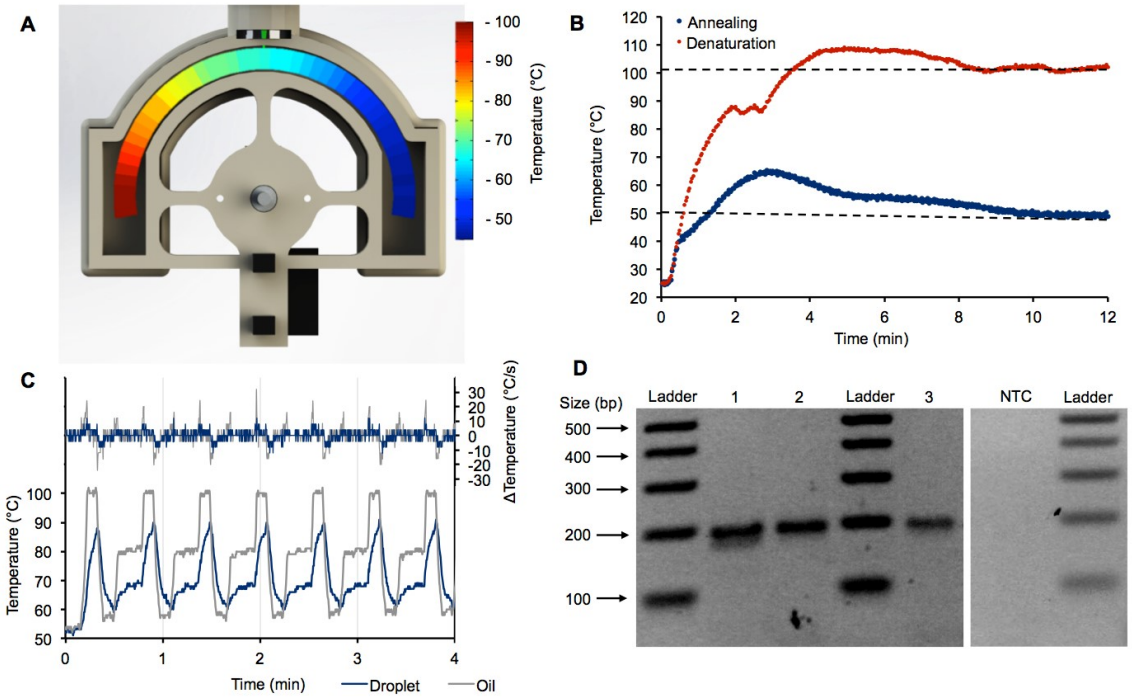

Fig. 2. Thermal characteristics and reproducibility of device. (**A**) Temperature color map of the heat gradient established between heaters with a maximum of 100°C on the left and a minimum of 45°C on the right. (**B**) Heat ramping of the two extreme temperature regions from 25°C to equilibrium within 10 min. (**C**) Representative thermocycling profile of the internal droplet temperature and surrounding oil temperature. Desired temperatures are consistently achieved even at sub-minute cycle times. The temperatures at each phase are 90.4 ± 0.2°C for denaturation, 68.4 ± 0.2°C for extension, and 60.2 ± 0.2°C for annealing. Droplet ramp rates up to 12°C/s and oil ramp rates up to 32°C/s are achieved by moving the droplet within the heat gradient. (**D**) Gel electropherogram showing the results from three successive trials (lanes 1–3) to amplify the 196 bp 16S rRNA V3 amplicon from 7 pg purified *K. pneumoniae* genomic DNA (equivalent to 1.4×10^3 genomic copies) and a no template control (NTC) sample. The thermocycling speed was 48 s/cycle, and 30 cycles were conducted. The band intensities in lanes 1–3 have a coefficient of variation of 4.0%.

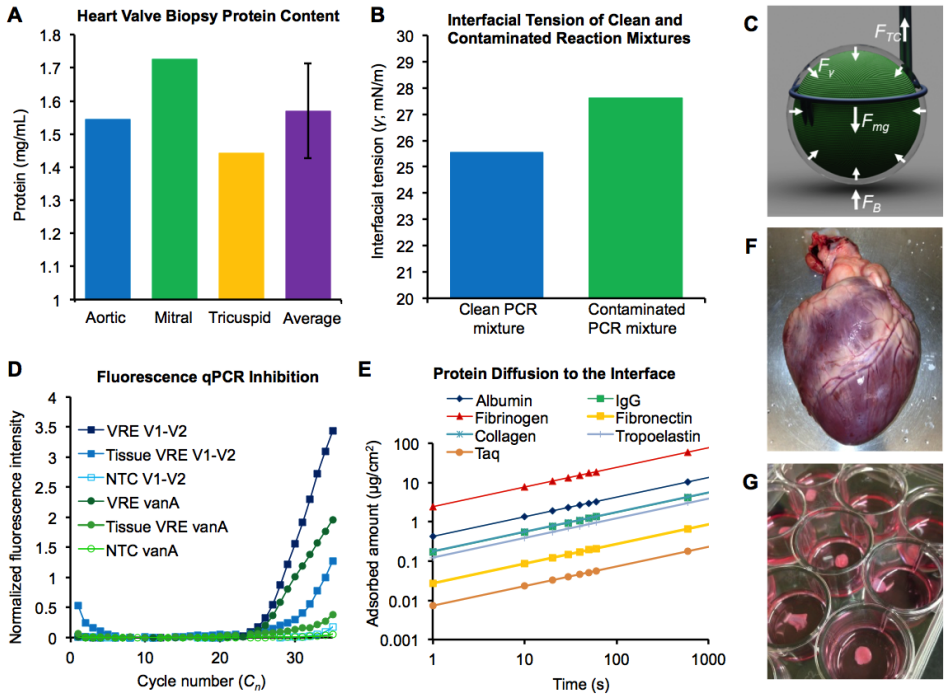

Fig. 3. Interfacial tension and fluorescence qPCR inhibition of the IE model. (**A**) Protein concentrations of the aortic, mitral, and tricuspid valve sections excised from a porcine heart and ground using a micro-mortar and -pestle. The total protein concentration of the tissue model is 1.6 ± 0.1 mg/mL. (**B**) Interfacial tensions (γ) of clean and contaminated PCR mixtures are 25.55 mN/m and 27.60 mN/m, respectively. (**C**) Free-body force diagram with the interfacial layer shown in clear. The forces on the droplet include the interfacial tension force (F_γ), the buoyancy force (F_B), the weight of the droplet (F_{mg}), and the thermocouple force (F_{TC}). (**D**) Fluorescence qPCR amplification curves for 16S rRNA hypervariable regions V1–V2 and *vanA* gene from intact vancomycin-resistant *Enterococcus faecium* (VRE) with and without tissue contamination. The C_t values for 16S rRNA V1–V2 without tissue, 16S rRNA V1–V2 with tissue, *vanA* without tissue**,** and *vanA* with tissue are 28.4, 30.0, 34.0, and 39.4, respectively. The tissue contamination inhibits fluorescence qPCR, as seen by the upward shift of 1.6 cycles for the 16S rRNA V1–V2 target and 5.4 cycles for the *vanA* target. Additionally, NTC samples for each primer set are plotted. (**E**) Protein diffusion to the interface is calculated based on typical blood and tissue concentrations using diffusivities from literature and Fick's equation. For comparison, the diffusion of *Taq* polymerase to the interface is also calculated. (**F**, **G**) The porcine heart, from which heart valves were excised, sectioned, inoculated, ground, and used as the PCR target.

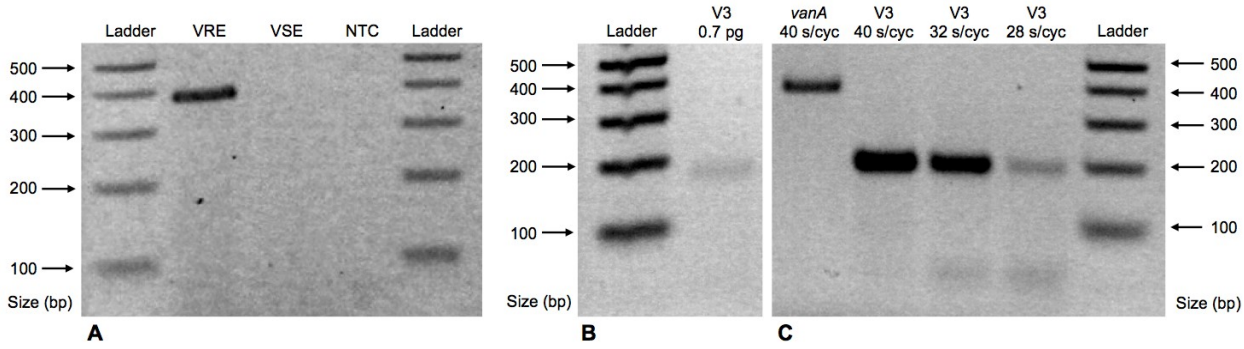

Fig. 4. Specificity, limit of detection, and speed of DOT thermocycling. (**A**) Gel electropherogram showing the differentiation of vancomycin-resistant *Enterococcus faecium* (VRE) and vancomycin-sensitive *Enterococcus faecalis* (VSE) by multiplexed amplification of the 377 bp *vanA* amplicon directly from bacterial culture. Simultaneous thermocycling was achieved by mounting three droplets on different thermocouples on the same motor arm. Lane 1: 1-kb plus DNA ladder; lane 2: VRE; lane 3: VSE; lane 4: no template control (NTC); and lane 5: 1-kb plus DNA ladder. (**B**) Gel electropherogram showing the limit of detection at the sub-picogram level by amplification of the 196 bp 16S rRNA V3 amplicon from 0.7 pg *K. pneumoniae* genomic DNA (equivalent to 1.4×10^2 genomic copies) at the speed of 48 s/cycle. Lane 1: 1-kb plus DNA ladder; and lane 2: 0.7 pg gDNA. (**C**) Gel electropherogram showing rapid amplification of the 16S rRNA V3 amplicon and *vanA* amplicon in the presence of tissue contaminants in 30 cycles. Lane 1: *vanA* amplified at 40 s/cycle (20 min) from 7×10^5 CFU VRE inoculated to valve tissue; V3 amplified from 7×10^5 CFU VRE inoculated to valve tissue, lane 2: at 40 s/cycle (20 min); lane 3: at 32 s/cycle (16 min); lane 4: at 28 s/cycle (14 min); and lane 5: 1-kb plus DNA ladder (see Fig. 2D for V3 NTC result).

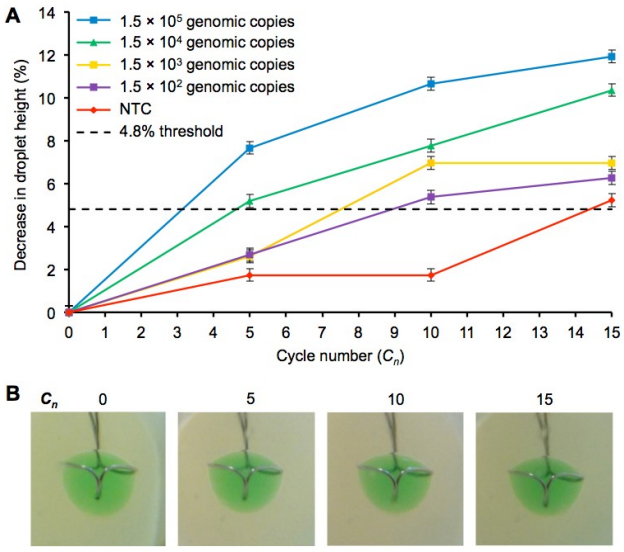

Fig. 5. Decrease in droplet height against cycle number. (**A**) Real-time detection of 16S rRNA amplification during early cycles by DOTS qPCR at a thermocycling speed of 48 s/cycle. Percent decrease in droplet height is plotted against C_n for amplifications from 750, 75, 7.5, and 0.75 pg genomic DNA (1.5×10^5, 1.5×10^4, 1.5×10^3, and 1.5×10^2 genomic copies, respectively) and no template control (NTC). Error bars represent overall device noise. A 4.8% threshold for detection is also plotted. The threshold was chosen to optimize the R^2 value of the linear regression shown in Figure 8. (**B**) Smartphone camera images of the droplet-on-

thermocouple submerged in oil. Images were taken every 5 thermal cycles and used to determine the droplet height.

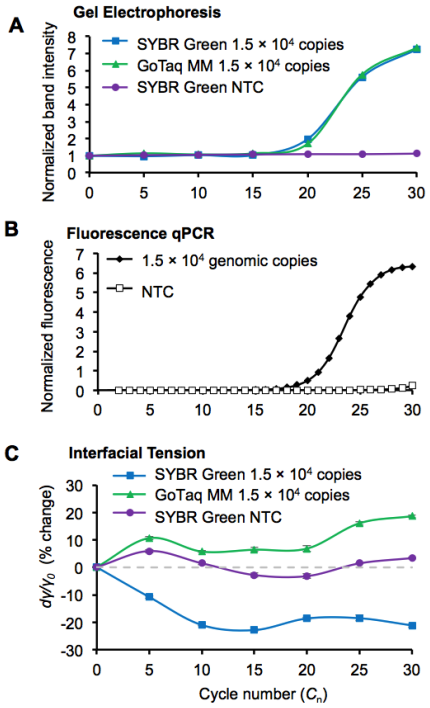

Fig. 6. Interfacial tension during DNA amplification in the presence of SYBR Green. Three reactions with different conditions were thermocycled in increments of five cycles. The reaction conditions were 1) 75 pg *K. pneumoniae* genomic DNA (1.5×10^4 genomic copies) with SYBR Green I (SG) to amplify the 16S rRNA V3 amplicon (196 bp), 2) 75 pg *K. pneumoniae* genomic DNA (1.5×10^4 genomic copies) without SG to amplify the 16S rRNA V3 amplicon (196 bp), and 3) no template control (NTC) with SG. The samples were analyzed by gel electrophoresis (Fig. S1). (**A**) Band intensities at the 196 bp region of the gel images were quantified, normalized to the intensity at C_0, and plotted against C_n. The product band is first detected at C_{20}, and no product band is detected for the NTC. (**B**) Fluorescence qPCR amplification curve for the 16S rRNA V3 amplicon (196 bp) amplified from 75 pg *K. pneumoniae* genomic DNA (1.5×10^4 genomic copies) and NTC. The C_t value is 21.11 ± 0.06. (**C**) The interfacial tensions of the PCRs were also analyzed with an FTÅ (First Ten Ångstroms) 200 contact angle and interfacial tension analyzer. The percent change in interfacial tension, $d\gamma/\gamma_0 = (\gamma_0 - \gamma_n)/\gamma_0$, is plotted against C_n. The γ of the reaction with DNA and SG decreases by 21% by C_{10} and remains the same thereafter. The γ of the reaction with DNA but without SG increases by 11% by C_5 and then further increases to 19% by C_{30}. The γ of the SG NTC reaction increases by 6% by C_5 and fluctuates within 4% thereafter.

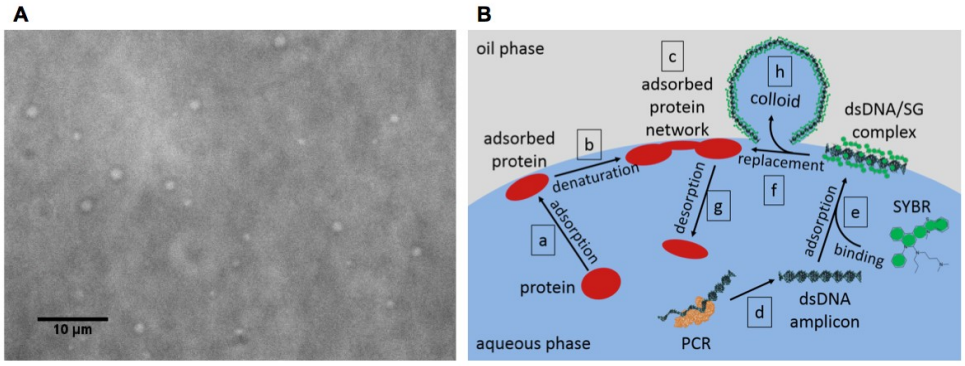

Fig. 7. Femtoliter water-in-oil droplets after DNA amplification with SYBR Green. (A) Bright-field microscope image showing water-in-oil droplets stabilized by dsDNA/SG complexes. The droplets range in diameter from 1–2 µm and in volume from 0.5–4.2 fL. These femtoliter droplets are observed in the oil phase following DNA amplification with SG. **(B)** Molecular schematic illustrating adsorption at the oil–water interface: a) protein adsorption initially stabilizes the droplet; b) proteins undergo conformational change; c) proteins form networks; d) PCR produces dsDNA amplicons; e) SG intercalates dsDNA, forming relatively hydrophobic complexes; f,g) dsDNA/SG complexes replace the surface-bound proteins because of high interfacial affinity and high concentration (Vroman effect); h) adsorption of dsDNA/SG complexes decreases interfacial tension, and colloidal suspensions become energetically favorable. Femtoliter water droplets are emulsified in the oil phase, decreasing droplet-on-thermocouple volume.

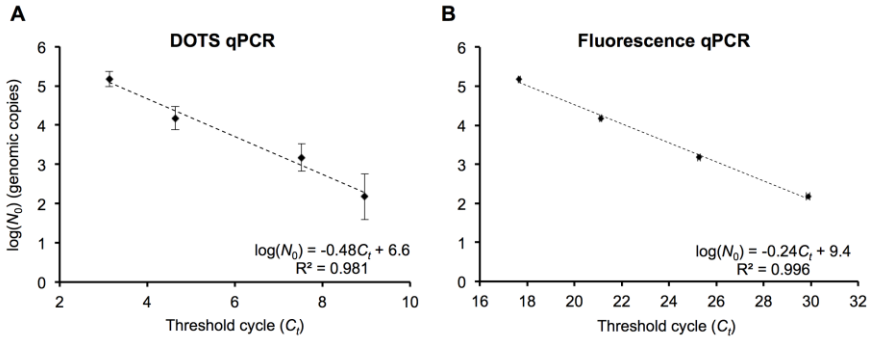

Fig. 8. Real-time PCR standard curves for DOTS qPCR and fluorescence qPCR. (**A**) DOTS qPCR standard curve for 16S amplification of the V3 amplicon from *Klebsiella pneumoniae* genomic DNA, in the range of 1.5×10^2 to 1.5×10^5 genomic copies. A trend line is fitted to the data by linear regression analysis: $\log(N_0) = -0.48C_t + 6.6$; $R^2 = 0.981$. In DOTS qPCR, the C_t values for NTC and 1.5×10^2, 1.5×10^3, 1.5×10^4, and 1.5×10^5 genomic copies are 14.4 ± 0.4, 9.0 ± 0.6, 7.5 ± 0.4, 4.6 ± 0.3, and 3.1 ± 0.2, respectively. (**B**) Fluorescence qPCR standard curve for 16S amplification of the V3 amplicon from *Klebsiella pneumoniae* genomic DNA, in the same range. A trend line is fitted to the data by linear regression analysis: $\log(N_0) = -0.24C_t + 9.4$; $R^2 = 0.996$. In fluorescence qPCR, the C_t values for NTC and 1.5×10^2, 1.5×10^3, 1.5×10^4, and 1.5×10^5 genomic copies are 32.4 ± 0.1, 29.88 ± 0.03, 25.28 ± 0.07, 21.11 ± 0.06, and 17.66 ± 0.04, respectively.

Table 1. Threshold cycles for DOTS qPCR and fluorescence qPCR. Uncertainties have been determined as the standard error of repeated measurements for DOTS qPCR and as the standard error of triplicate experiments for fluorescence qPCR.

N_0 (genomic copies)	DOTS qPCR C_t	Fluorescence qPCR C_t
1.5×10^5	3.1 ± 0.2	17.66 ± 0.04
1.5×10^4	4.6 ± 0.3	21.11 ± 0.06
1.5×10^3	7.5 ± 0.4	25.28 ± 0.07
1.5×10^2	9.0 ± 0.6	29.88 ± 0.03
NTC	14.4 ± 0.4	32.4 ± 0.1